

The [O III] λ 5007 equivalent width distribution at $z \sim 2$: the redshift evolution of the extreme emission line galaxies

Kristan N. K. Boyett ^{1,2,3}★ Daniel P. Stark,⁴ Andrew J. Bunker,¹ Mengtao Tang ^{4,5}
and Michael V. Maseda ⁶

¹Department of Physics, University of Oxford, Denys Wilkinson Building, Keble Road, Oxford OX1 3RH, UK

²School of Physics, Tin Alley, University of Melbourne, Melbourne, VIC 3010, Australia

³ARC Centre of Excellence for All Sky Astrophysics in 3 Dimensions (ASTRO 3D), Canberra 2611, Australia

⁴Department of Astronomy/Steward Observatory, University of Arizona, 933 N Cherry Avenue, Tucson, AZ 85721 USA

⁵Department of Physics and Astronomy, University College London, Gower Street, London WC1E 6BT, UK

⁶Department of Astronomy, University of Wisconsin-Madison, 475 N. Charter St., Madison, WI 53706 USA

Accepted 2022 April 12. Received 2022 April 8; in original form 2021 October 22

ABSTRACT

We determine the [O III] λ 5007 equivalent width (EW) distribution of $1.700 < z < 2.274$ rest-frame ultraviolet (UV)-selected ($M_{\text{UV}} < -19$) star-forming galaxies in the GOODS North and South fields. We make use of deep HDUV broad-band photometry catalogues for selection and 3D-*HST* WFC3/IR grism spectra for measurement of line properties. The [O III] λ 5007 EW distribution allows us to measure the abundance of extreme emission line galaxies (EELGs) within this population. We model a lognormal distribution to the [O III] λ 5007 rest-frame EWs of galaxies in our sample, with location parameter $\mu = 4.24 \pm 0.07$ and variance parameter $\sigma = 1.33 \pm 0.06$. This EW distribution has a mean [O III] λ 5007 EW of $168 \pm 1 \text{ \AA}$. The fractions of $z \sim 2$ rest-UV-selected galaxies with [O III] λ 5007 EWs greater than 500, 750, and 1000 \AA are measured to be $6.8^{+1.0}_{-0.9}$ per cent, $3.6^{+0.7}_{-0.6}$ per cent, and $2.2^{+0.5}_{-0.4}$ per cent, respectively. The EELG fractions do not vary strongly with UV luminosity in the range ($-21.6 < M_{\text{UV}} < -19.0$) considered in this paper, consistent with findings at higher redshifts. We compare our results to $z \sim 5$ and $z \sim 7$ studies, where candidate EELGs have been discovered through *Spitzer*/IRAC colours, and we identify rapid evolution with redshift in the fraction of star-forming galaxies observed in an extreme emission line phase (a rise by a factor ~ 10 between $z \sim 2$ and $z \sim 7$). This evolution is consistent with an increased incidence of strong bursts in the galaxy population of the reionization era. While this population makes a sub-dominant contribution of the ionizing emissivity at $z \simeq 2$, EELGs are likely to dominate the ionizing output in the reionization era.

Key words: galaxies: evolution – galaxies: high-redshift.

1 INTRODUCTION

Over the last decade, considerable effort has focused on the study of extreme emission line galaxies (EELGs). These systems are often identified through their large [O III] or H β equivalent widths (EWs) and have been studied in detail at very low redshift (Cardamone et al. 2009; Amorín, Pérez-Montero & Vílchez 2010; Izotov, Guseva & Thuan 2011; Brunner et al. 2020) and in comparable populations at redshifts $z \sim 1 - 3$ (e.g. Atek et al. 2011; van der Wel et al. 2011; Amorín et al. 2015; Maseda et al. 2018; Tang et al. 2019; Du et al. 2020; Onodera et al. 2020). Although rare at the current epoch, EELGs are thought to represent a significant fraction of the star-forming galaxy (SFG) population at $z > 6$ (e.g. Smit et al. 2015; De Barros et al. 2019; Endsley et al. 2021). They are characterized by a combination of strong nebular line emission and weak rest-optical continuum (i.e. high EW), as expected for a galaxy powered by a very young stellar population with moderately low metallicity.

These systems thus provide a signpost of low-mass galaxies as they go through an upturn or burst of star formation.

In the last few years, spectroscopic studies at $z \sim 0 - 2$ have shown that EELGs are more efficient ionizing agents than typical SFGs at these epochs. The production efficiency of ionizing radiation ξ_{ion} [the measure of the production rate of ionizing photons per unit far-ultraviolet (UV) luminosity for a galaxy] increases with [O III] λ 5007 EWs, reaching its largest values in the most extreme systems within the EELG population (e.g. Chevillard et al. 2018; Tang et al. 2019; Onodera et al. 2020). Many EELGs also show evidence of large ionizing photon escape fractions, f_{esc} (the fraction of HI ionizing photons that reach the inter-galactic medium (IGM), e.g. Izotov et al. 2016; Fletcher et al. 2019). Nebular gas under extreme ionization conditions has been proposed as a necessary but not sufficient criterion for large f_{esc} (Izotov et al. 2018; Jaskot et al. 2019; Nakajima et al. 2020). The ionizing conditions are commonly parametrized using the O32 index (the flux ratio of [O III] $\lambda\lambda$ 4959,5007 and [O II] $\lambda\lambda$ 3726,3729), a quantity that will soon be measurable at $z > 6$ with *JWST*. Nakajima et al. (2020) find that $\text{O32} > 6$ is a necessary condition for large f_{esc} (galaxies with

* E-mail: kit.boyett@unimelb.edu.au

$f_{\text{esc}} > 0.1$), and Izotov et al. (2016) report similar results (although Naidu et al. 2018, Bassett et al. 2019, and Ramambason et al. 2020 note large scatter in the relation between O32 and f_{esc}). Such high values of O32 are uniquely found in EELGs, in particular those systems with $[\text{O III}]\lambda 5007$ EW $> 750 \text{ \AA}$ (e.g. Tang et al. 2019; Onodera et al. 2020; Sanders et al. 2020). At $z \sim 3$, Pahl et al. (2021) measure an average f_{esc} for SFGs to be ~ 6 per cent (Begley et al. 2022 recently determine a consistent value of 7 ± 2 per cent). In contrast, individual EELGs with $[\text{O III}]\lambda 5007$ EW well above 1000 \AA have been observed to exhibit escape fractions up to an order of magnitude greater than these typical systems (Vanzella et al. 2016; Rivera-Thorsen et al. 2017; Izotov et al. 2018; Fletcher et al. 2019). These observations suggest that when galaxies are in an EELG (or burst) phase, they are likely to contribute more to the ionizing background than a typical SFG at $z \simeq 2 - 3$. However, the fraction of EELGs in the star-forming population is not well constrained at these redshifts. As a result, it is not clear that these systems make a significant contribution to the $z \simeq 2 - 3$ ionizing background.

At higher redshifts ($z > 5$), broad-band spectral energy distributions (SEDs) suggest that EELGs may be fairly ubiquitous within the SFG population. This inference comes from the presence of strong *Spitzer*/IRAC flux excesses in filters that are contaminated by $[\text{O III}] + \text{H}\beta$ emission lines. (e.g. Labbé et al. 2013). The flux excesses imply substantial EWs, often placing galaxies in the EELG regime. While for some of these $z > 5$ galaxies, the flux excess may also have a contribution from a Balmer break (e.g. Eyles et al. 2005, 2007; Roberts-Borsani, Ellis & Laporte 2020), over some redshift ranges (e.g. $6.6 < z < 6.9$, Smit et al. 2014, 2015; Endsley et al. 2021) the flux excess can unambiguously be linked to rest-optical emission lines. This has enabled the first glimpse at the $[\text{O III}] + \text{H}\beta$ EW distribution in the reionization era. At $z > 6$, typical $[\text{O III}] + \text{H}\beta$ rest-frame EWs are $\sim 600\text{--}700 \text{ \AA}$ (Labbé et al. 2013; De Barros et al. 2019; Endsley et al. 2021). Endsley et al. (2021) find that 20 per cent of the SFG population at $z \sim 7$ exhibits yet more extreme EWs with $[\text{O III}] + \text{H}\beta$ EW $> 1200 \text{ \AA}$ (see also Smit et al. 2014, 2015; Roberts-Borsani et al. 2016; Castellano et al. 2017). Like EELGs at lower redshifts, these large EWs imply the presence of extreme radiation fields, which is further supported by observations of strong line emission from high-ionization rest-UV metal lines, such as $\text{C III}] \lambda 1909 \text{ \AA}$, $\text{C IV} \lambda 1549 \text{ \AA}$ and $\text{He II} \lambda 1640 \text{ \AA}$ (Laporte et al. 2017; Mainali et al. 2017; Schmidt et al. 2017; Stark et al. 2017, 2015a, b; Mainali et al. 2018; Hutchison et al. 2019).

SFGs are expected to contribute the bulk of the ionizing photon budget during the reionization epoch (e.g. Bunker et al. 2004, 2010; Bouwens et al. 2015b; Robertson et al. 2015; Stanway, Eldridge & Becker 2016; Stark 2016; Boylan-Kolchin 2018; Naidu et al. 2020; Finkelstein et al. 2019; c.f., Madau & Haardt 2015). With a large fraction of early galaxies exhibiting extreme $[\text{O III}] + \text{H}\beta$ EWs, it is likely that a significant proportion of the ionizing output responsible for reionizing the IGM comes from SFGs in an EELG or burst phase. Galaxies may also be very effective at producing globular clusters and young massive star clusters during these intense star formation episodes (Vanzella et al. 2022, 2020; Endsley et al. 2021). It is clear that EELGs are likely to play an important role in galaxy growth and reionization. While existing data hint at the EELG phase becoming more common towards higher redshifts, we currently do not have quantitative constraints on how the prevalence of this population evolves with redshift or varies with galaxy luminosity. This not only hinders our ability to track the contribution of galaxies to reionization, but it also impedes our understanding of how burstiness may be changing in the galaxy population.

In this paper, we seek to provide a robust measurement of the $[\text{O III}]\lambda 5007$ EW distribution in SFGs at $z \simeq 2$. By selecting our systems in the same manner as those at higher redshifts (i.e. UV-selected dropouts), we aim to provide a baseline measurement which allows the evolution of the EELG population to be established as a function of redshift into the epoch of reionization (EOR). We select galaxies at $z \sim 1.7 - 2.3$ using the HDUV (Hubble Deep UV) photometric catalogues (Oesch et al. 2018), and we characterize the $[\text{O III}]\lambda 5007$ emission line properties using 3D-*HST* slitless spectra (Momcheva et al. 2016; described in Section 2). In Section 3, we determine whether the fraction of the strongest line emitters increases with redshift by comparing our results at $z \sim 2$ with existing measurements at higher redshifts. We discuss implications of our results for reionization in Section 4. Throughout this paper, we assume a Λ -dominated, flat universe with $\Omega_{\Lambda} = 0.7$, $\Omega_M = 0.3$, and $H_0 = 70 \text{ km s}^{-1} \text{ Mpc}^{-1}$. All EWs are quoted in the rest-frame and all magnitudes are given in the AB system (Oke & Gunn 1983).

2 SAMPLE SELECTION

2.1 A photometric sample of $z \simeq 1.7 - 2.3$ galaxies

Our paper is motivated by recent studies $z \sim 7$ that have revealed intense rest-optical nebular emission (e.g. median $[\text{O III}] + \text{H}\beta$ EW $\sim 600 - 700 \text{ \AA}$, see Labbé et al. 2013; De Barros et al. 2019; Endsley et al. 2021). While examples of such objects have been identified at lower redshifts ($z \sim 1 - 3$ Atek et al. 2010; Fumagalli et al. 2012; Maseda et al. 2018), the fraction of SFGs with extreme line emission at these redshifts is yet to be quantified. In this paper, we combine the *HST*/WFC3 G141 grism slitless spectroscopy from 3D-*HST* (Momcheva et al. 2016) with the HDUV legacy survey photometry (Oesch et al. 2018) to measure the EW distribution of $[\text{O III}]\lambda 5007$ of 671 galaxies at redshift ~ 2 ($1.700 < z < 2.274$). We describe the selection criteria that lead to this sample below.

To facilitate comparison to higher redshift $[\text{O III}] + \text{H}\beta$ EW distributions (e.g. De Barros et al. 2019; Endsley et al. 2021), we select our parent sample from HDUV catalogues (Oesch et al. 2018) using a rest-UV Lyman break dropout colour selection that is similar in nature to those used at $z > 4$. We note that many commonly used broad-band photometric catalogues in these fields are publicly available (e.g. Skelton et al. 2014; Barro et al. 2019; Merlin et al. 2021), and the characteristic imprint of the Lyman- α spectral break on the broad-band photometry has been used to successfully identify galaxies at redshifts typically above $z > 3$ (see also Bouwens, Illingworth & Oesch 2015a, Finkelstein, Ryan & Papovich 2015 at high redshift). To obtain a sample of galaxies selected using this Lyman break at lower redshifts ($z \sim 2$) requires additional broad-band photometry at shorter wavelengths (in the UV), which has only recently been made publicly available in the HDUV catalogue. We rely upon the HDUV catalogue as opposed to other successful data sets because of the unique leverage that the UV photometry provides in covering the Lyman break below $z < 3$ for the purpose of deriving good photometric redshifts using the same technique that has been used on samples at higher redshift which we will compare against. The HDUV catalogue adds UV photometry in the *HST*/WFC3-UVIS F275W and F336W filters over $\sim 100 \text{ arcmin}^2$ of the CANDELS GOODS North and South fields. The addition of UV photometry to existing optical and near-infrared (NIR) data in these fields allows selection of $z \sim 2$ galaxies using their characteristic Lyman break (Steidel et al. 1996b, a) providing robust photometric redshifts. The two UV filters have average 5σ magnitude depths (in 0.4 diameter apertures) of 27.4(27.6) and 27.8(28.0) for F275W and F336W across

GOODS North(South) (Oesch et al. 2018). These two UV filters are combined with the high-quality *HST* ACS optical and WFC3 NIR photometry, as well as the *Spitzer*/IRAC and ground-based filters. Oesch et al. (2018) use this photometry to generate photometric redshifts for the 30 561 galaxies in the HDUV catalogue using EAZY (Brammer, van Dokkum & Coppi 2008; using the same procedures as described in Skelton et al. 2014). As we describe below, we construct our sample using these photometric redshifts as our initial selection, similar to that often used to identify $z > 4$ galaxies (e.g. McLure et al. 2011; Finkelstein et al. 2015). At the redshifts, we are interested in for this analysis, the photometric redshifts are primarily driven by the Lyman break probed by the HDUV photometry. For the galaxies in our sample, we find that the HDUV photometric redshifts are in reasonable agreement with those from Skelton et al. (2014; which did not have access to the U-F275W/UV-F336W *HST* WFC3-UVIS broad-band filters) and that the additional UV photometry available in the HDUV survey improves the constraints on photometric redshifts. For the galaxies in our sample, we find the HDUV photometric redshift uncertainties are typically smaller than those determined by Skelton et al. (2014) by roughly 21 per cent.

Since our goal is to characterize the strength of the [O III] λ 5007 emission in these galaxies, we must pick objects that have photometric redshifts which place the [O III] doublet confidently within the G141 grism spectral window ($\sim 1.0755\text{--}1.6999 \mu\text{m}$). This translates into a redshift range of $1.148 < z < 2.395$. However, there is an additional constraint that limits our selection further. Below $z \sim 1.7$, the Lyman limit begins to shift blueward of the F275W and F336W filters, making dropout identification somewhat less reliable without bluer filters (i.e. F225W). We thus adopt $z = 1.700$ as our lower redshift bound. At the high redshift end, we need to choose objects that are confidently within the redshift range ($z < 2.395$), where we can measure the [O III] doublet with the G141 grism. Accounting for the typical photometric redshift uncertainty in this sample, we conservatively adopt an upper redshift bound of $z = 2.274$ for photometric selection, minimizing the inclusion of sources with true redshifts above the $z = 2.395$ threshold. We select all galaxies in the HDUV catalogues with photometric redshifts between 1.700 and 2.274. As we will discuss below, sources in this redshift range have SEDs that show strong breaks associated with IGM attenuation, driving the solution of the photometric redshifts in HDUV catalogue. This redshift cut results in a sample of 4026 galaxies.

We next apply a brightness cut on the rest-UV magnitudes of the photometric sample. This serves two purposes. First, it ensures consistency with higher redshift dropout samples that are traditionally selected in the rest-frame UV. Secondly, the magnitude threshold guarantees that our sample is well-matched to the sensitivity of the grism spectra, enabling useful constraints (or upper limits) on the [O III] λ 5007 EW. We adopt a fixed cut on M_{UV} , the absolute magnitude measured near rest-frame 1500 Å. To calculate M_{UV} for our sample, we adopt the apparent magnitude in the filter closest to rest-frame 1500 Å. We use either the observed F435W (B-band) magnitude below a redshift of $z = 2.2$ or the observed F606W (V-band) magnitude above $z = 2.2$. To convert apparent to absolute magnitude, we use the grism-based redshift if the [O III] doublet is detected at $S/N > 5$ and the photometric redshift otherwise. We will show below that the grism redshifts and photometric redshifts are highly consistent. We choose $M_{UV} = -19$ as our magnitude cut, ensuring that galaxies are detected at significantly greater than 5σ in both F435W and F606W filters. This reduces the sample to 766 galaxies. The exact choice of the M_{UV} threshold is arbitrary and does not significantly change our best-fitting parameters for the EW

distribution, as discussed further in Section 3.4. The M_{UV} distribution for our final sample is shown in Fig. 1.

We use the latest grism catalogue (V4.1.5) from 3D-*HST* (Momcheva et al. 2016; Brammer et al. 2012). This catalogue contains spectra extracted for all galaxies within the field with a NIR JH_{IR} magnitude (derived from the $J_{125} + JH_{140} + H_{160}$ combined detection image; see Momcheva et al. 2016) brighter than 26. There are 28 galaxies within our sample that do not satisfy this NIR threshold and hence do not have available spectroscopic data. To retain these targets within our sample, we locate each within the grism slitless spectroscopy and inspect their 2D spectrum, determining that no emission lines were visible in any of the 28 systems. The lack of any visible emission lines is confirmed by utilizing an alternative line detection procedure (with no requirements on NIR magnitude) described in Maseda et al. (2018). We will treat each as a non-detection in the following analysis. Keeping these targets within our sample ensures that the NIR magnitude never directly enters our selection, which is important owing to the influence that emission lines can have on the NIR broad-band flux if EWs are large.

We make two final cuts to our photometric sample. First, we remove a small number of sources with very red colours. Such objects are generally excluded from Lyman break selections and would not feature in higher redshift samples we wish to compare to. To remove these objects, we utilize a colour cut of $B - V < 0.8$ (using the F435W and F606W *HST* ACS filters). This colour threshold is very close to the Lyman break colour cut used at similar redshifts by Oesch et al. (2018). This specific colour is chosen to correspond to sources with $E(B-V) < 0.4$, equivalent to UV slopes with $\beta < -1.0$ (where $f_{\lambda} \propto \lambda^{\beta}$). Here, we have assumed the dust attenuation law derived from typical $z \sim 2$ galaxies from Reddy et al. (2015). This B-V threshold reveals four very red sources that we remove from our sample. We note that adopting a slightly different colour cut does not significantly alter our results. We also wish to remove sources that may host active galactic nuclei, as our goal is to establish the [O III] λ 5007 EW distribution in SFGs. We cross-match our sample against deep *Chandra* X-ray imaging across GOODS-N (Alexander et al. 2003; Xue et al. 2016) and GOODS-S (Xue et al. 2011; Luo et al. 2017), identifying sources that match the coordinates of our sample using a $1''$ search radius. There are 31 targets within our sample that show X-ray counterparts and are removed. Together, these two cuts reduce our sample to 731 galaxies.

Our goal is to establish the [O III] λ 5007 EW distribution in this photometric sample. To do so, we first need to ensure that we have removed any galaxies with grism artefacts from our sample, and secondly, we need to quantify the scatter between the photometric and grism redshifts. We visually examine the grism spectra of our remaining sample to characterize data quality. We identify spectra that have artificial features created by edge effects where the dispersed light of the galaxy falls partially outside the illuminated region of the detector. These artificial features may be mistaken for emission lines, while regions of un-illuminated spectra may contain genuine features that would be missed. The 3D-*HST* catalogue provides a flag ‘*f_cover*’ describing the fraction of dispersed light that falls within the illuminated region of the detector. We find that removing all sources where the *f_cover* parameter is below 0.65 effectively eliminates these incidences in our sample. This removes 51 targets.

We also identify targets that display a negative spectrum on average, where poor contamination subtraction of the contributed light from overlapping spectra has compromised the individual extractions. The 3D-*HST* catalogue flag ‘*f_negative*’ describes the fraction of the spectrum that has a negative flux and we determine

that a cut on the `f_negative` parameter at 0.7 effectively removes these compromised spectra from our sample, eliminating further four galaxies. We additionally review and remove one further system (3D-*HST* ID S24717) identified to have incorrectly associated grism emission lines, due to the dispersed light of other galaxies lying coincident with that of the target. We deem the target spectrum to be irretrievable behind the dominant contamination of the neighbour and remove it from the sample. We also individually review all targets with SExtractor '`class_star`' value greater than 0.5. This inspection results in three targets being removed (S20271, S23225, and S29694) after being identified as either stars or for having their photometry or slitless spectroscopy compromised by lying in the wings of stellar diffraction spikes. We also remove one object (S24312) as it is associated with one component of a larger galaxy that is already in our sample (S24365). These cuts leave 671 galaxies.

2.2 Photometric redshifts and contaminants

Now that we have a cleaned sample of grism spectra, we can quantify the reliability of the photometric redshifts used to select our parent sample and assess the contamination level among those objects without spectroscopic redshifts. To do so, we take two different approaches. First, we identify objects with robust grism redshifts in our photometric sample. We define these as those with confident emission line detections ([O III] doublet detected at a greater than 5σ significance) following work in Tang et al. (2019). There are 293 galaxies that satisfy this emission line cut in our photometric sample. In this sub-sample, we see that the photometric redshifts do a very good job of reproducing the grism redshifts. To quantify this, we define the typical scatter between photometric and grism redshift using the normalized median absolute deviation, defined as $\sigma_{\text{NMAD}} = 1.48 \times \text{median}(|\Delta z - \text{median}(\Delta z)| / (1 + z_{\text{spec}}))$, where $\Delta z = z_{\text{spec}} - z_{\text{phot}}$ (e.g. Brammer et al. 2008). We find a normalized median absolute deviation of $\sigma_{\text{NMAD}} = 0.037$ for the sub-sample with robust grism redshifts, suggesting good agreement between photometric and grism redshifts. We will assume this dispersion between spectroscopic and photometric redshifts is characteristic of our total sample, including those systems lacking grism redshifts. This latter subset primarily includes objects with slightly lower EW emission lines. The HDUV photometric redshift 68 per cent confidence intervals of these sources (median $\Delta z = 0.063$) are comparable to those objects in our sample with grism redshifts (median $\Delta z = 0.053$), likely reflecting their similar continuum magnitudes which in turn enable robust characterization of the Lyman break (which again is what primarily drives the photometric redshift solution). The average strength of the Lyman break is consistent between the robust grism redshift sub-sample and the sub-sample without significant line detections, both exhibiting a strong F275W-F435W mean break colour of 2.4 mag. Hence, in spite of their lower emission line EWs, we expect the photometric redshifts of these sources to be similar in their reliability as those with grism redshifts.

The typical dispersion between photometric and grism redshifts allows us to calculate the fraction of our sample that is likely to be in-scattered from redshifts where the G141 grism is not able to constrain [O III] emission ($z < 1.148$ or $z > 2.395$). Given the value of σ_{NMAD} , we can perturb the measured photometric redshifts of our sample to quantify this contamination rate. While the in-scatter rate from sources with $z < 1.148$ is expected to be negligible (owing to the significant buffer provided by our $z > 1.700$ selection), the dispersion between grism and photometric redshifts suggests that 3.4 per cent of our photometric sample will have true redshifts of

$z > 2.395$. These sources will not show detections of [O III] even though they could have strong nebular line emission. This is easily accounted for in the derived EW distribution, as we will discuss in Section 3.

In addition to the typical scatter described above, we expect a small number of catastrophic outliers, where the derived photometric redshift is substantially offset from the true redshift of the object. Such objects are generally not included in the Gaussian distribution with $\sigma = \sigma_{\text{NMAD}}$, so they must be considered separately. Contaminants can be identified in the G141 grism via detection of strong rest-optical lines ($H\alpha$, [OII], or [O III]) at redshifts well outside of our selected range ($1.700 < z < 2.274$) or through the extensive ground-based spectroscopy that has been conducted in the GOODS fields. We first consider the latter and focus on the GOODS South field where many public redshift surveys have been conducted (e.g. Le Fèvre et al. 2005; Vanzella et al. 2008; Balestra et al. 2010; Kurk et al. 2013; Le Fèvre et al. 2015; Garilli et al. 2021; Inami et al. 2017). We cross-match these surveys with our GOODS-South catalogue (317 galaxies), finding 116 unique matches. The spectra in these catalogues find only one catastrophic outlier with a confident redshift identification (3D-*HST* ID: 19233, matched to Balestra et al. 2010 ID: J033227.25-274919.2 with $z_{\text{spec}} = 0.5568$), indicating a catastrophic outlier fraction of 0.96 per cent in the ground-based spectra and suggesting a fraction of at least 0.3 per cent in our total GOODS-S sample. The WFC3/IR grism spectra provide an independent check. The G141 grism is able to detect $H\alpha$ down to $z = 0.6$, providing a window on low- z interlopers in our sample. Here, we define a catastrophic outlier as a source with a redshift that is further than $5\sigma_{\text{NMAD}}$ from our lower redshift bound, corresponding to $z = 1.2$. We identify 10 sources with $H\alpha$ detections, but none fall below $z = 1.4$. These redshifts are consistent with the Gaussian distribution implied by our calculation of σ_{NMAD} , hence the grism sample is also suggestive of a low catastrophic outlier rate. In the following section, we will conservatively assume a catastrophic outlier rate of 1.3 per cent within our sample. We will add this catastrophic contamination fraction to that derived for more typical source-to-source redshift scatter. The total contamination fraction (3.4 per cent + 1.0 per cent = 4.4 per cent) will be modelled when deriving the EW distribution.

To summarize, we are left with a final sample of 671 galaxies, with 354 in GOODS North and 317 in GOODS South. The total photometric sample includes 293 systems with $\geq 5\sigma$ detections of the [O III] doublet. The photometric redshift distribution is presented in Fig. 2 with a medium value of $z = 2.0$. The absolute M_{UV} magnitude distribution is shown in Fig. 1 and spans $-21.6 < M_{\text{UV}} < -19.0$, with 75.6 per cent of targets fainter than $M_{\text{UV}} = -20.0$. These values are well-matched to those of $z \simeq 7$ galaxies that have been used to infer [O III] + $H\beta$ EWs via *Spitzer*/IRAC excesses (De Barros et al. 2019; Endsley et al. 2021).

3 [O III] λ 5007 EQUIVALENT WIDTH DISTRIBUTION AT $z \sim 2$

In this section, we compute the [O III] λ 5007 EW distribution at $z \sim 2$ from our selected sample. We first discuss measurements of individual EWs in Section 3.1 and then describe how we characterize the functional form of the EW distribution in Section 3.2. From this distribution, we measure the fraction of galaxies caught in an extreme EW phase (the EELG fraction), corresponding to very large specific star formation rates (sSFR) expected when galaxies experience bursts of star formation. We characterize the redshift and

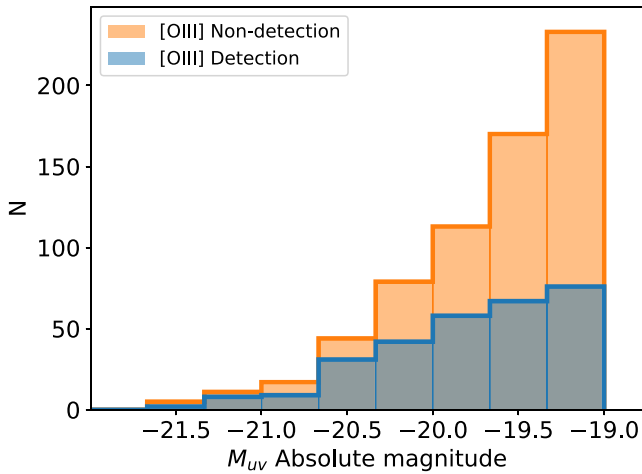


Figure 1. Absolute magnitude distribution of the photometric sample we use for our [O III] EW distribution, split into those with (blue) and without (orange) [O III] doublet detections. We apply an absolute magnitude threshold of $M_{UV} = -19$ to our sample.

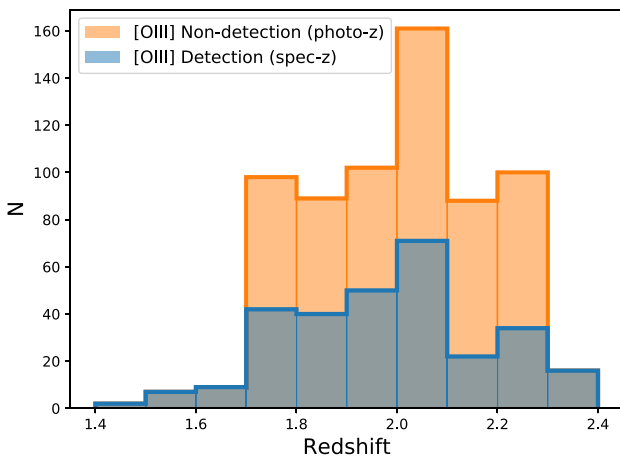


Figure 2. The redshift distribution of the parent sample for our [O III] EW distribution, split into spectroscopic redshifts (blue) if the [O III] doublet was detected and photometric redshifts (orange) if not. The sample includes 671 $z \simeq 2$ galaxies in the combined GOODS North and South fields. All the systems are selected to have HDUV photometric redshift in the range $1.700 < z < 2.274$ (Oesch et al. 2018) and absolute magnitude brighter than $M_{UV} = -19$. Scatter between the spectroscopic and photometric redshifts means that a small number of galaxies have spectroscopic redshifts, which fall slightly outside the photometric-redshift-based range of $1.700 < z < 2.274$.

luminosity dependence of the EELG fraction in Sections 3.3 and 3.4, respectively.

3.1 Individual equivalent width measurements

The first step in deriving the [O III] λ 5007 EW distribution is to robustly measure the individual EWs for each of the 671 galaxies in our final sample. As described in Section 2, we create a sub-sample of galaxies with significant [O III] doublet detections ($\geq 5\sigma$) and determine their [O III] λ 5007 EW. For the remaining sample, we derive upper limits on the EW. We describe this procedure below.

Our approach to line measurement is similar to that taken in Tang et al. (2019). For galaxies with a $\geq 5\sigma$ [O III] doublet detection in the grism spectra of Momcheva et al. (2016), we use their measured line

flux in determining the EW. We note that the [O III] λ 4959, 5007 Å doublet is unresolved at the spectral resolution of the G141 grism and the total [O III] doublet flux is reported in Momcheva et al. (2016). We correct the total line flux of the doublet to the expected line flux of [O III] λ 5007 alone, assuming the theoretical line flux ratio of 2.98 between [O III] λ 5007 Å and [O III] λ 4959 Å (Storey & Zeippen 2000). For the estimate of the stellar continuum at the observed wavelength, we derive the continuum flux density from the broad-band photometry rather than using the spectral continuum measured from the grism spectra by Momcheva et al. (2016). In many objects in our sample, the continuum is often very low S/N. This approach allows us to have a uniform method for our entire sample, and as we show later in this section the two approaches give consistent EW measurements. To compute the photometric broad-band flux density in the filter covering the [O III] doublet, we compute the continuum flux using an aperture that is matched to the grism spectral extraction aperture for each source. The F125W broad-band filter is used to determine the continuum for galaxies below $z = 1.8$, the F140W filter is used in the range $z = 1.8$ –2 and the F160W filter is used above $z = 2$ (or above $z = 1.8$ when F140W is unavailable). In determining the continuum flux density from the broad-band photometry, we correct the flux within the filter for the contribution of emission lines. We consider the contribution from all lines detected in the grism spectra, weighted by the filter transmission profile at the respective location of each line. For the majority of sources in our sample, this is a very small correction that does not significantly impact the EW inference. We verify that systems with grism non-detections have minimal emission line contribution to the broad-band flux (< 5 per cent). We find that three sources in our sample are sufficiently line-dominated that the derived continuum flux density (after line subtraction) lies below the 5σ flux density limit for that filter. In these cases (S19339, S30532, and N16381), we utilize the average of neighbouring broad-band filters without line contamination to measure the continuum flux density. Finally, we inspect, by-eye, all galaxies where the Skelton et al. (2014) half-light radii of the target and a nearby neighbour overlap. Two targets of concern are identified, and we employ Galfit (Peng et al. 2002) to model and subtract the contribution from the neighbour to the continuum flux density.

In order to compute the [O III] λ 5007 EW, we must make a small correction to convert the continuum flux density at the effective wavelength of the chosen filter (i.e. F125W, F140W, F160W) to that at the rest-wavelength of [O III] λ 5007. Given the small wavelength baseline involved, we assume that the continuum is flat in f_ν , as is appropriate for unreddened stellar populations at the range of ages spanned by our sample (e.g. van der Wel et al. 2011; Maseda et al. 2014). This correction is no more than 10 per cent, and changes by less than 1 per cent if we consider galaxies with more reddening (i.e. selective extinction of $E(B-V) = 0.2$ with a Calzetti reddening curve). The [O III] λ 5007 EW is then taken as the ratio of the line flux to the continuum flux density and corrected to the rest-frame using the grism-measured spectroscopic redshift ($EW_{rest} = EW_{obs}/(1+z)$).

For systems lacking [O III] doublet detections with $S/N \geq 5$, we derive 5σ upper limits on the [O III] λ 5007 EW. For each non-detection, we adopt the 5σ grism flux upper limit using the line sensitivity equation, described in Momcheva et al. (2016). This is an empirical parametrization of the flux uncertainties determined through 2D model fitting of the grism spectra, acting as a function of the filter transmission throughput at the observed wavelength and the aperture size required to span the spatial extent of the galaxy (for each object we adopt the broad-band flux radius from Skelton et al. 2014). The EW 5σ upper limits are then produced by combining the line flux upper limit with the broad-band continuum (derived as

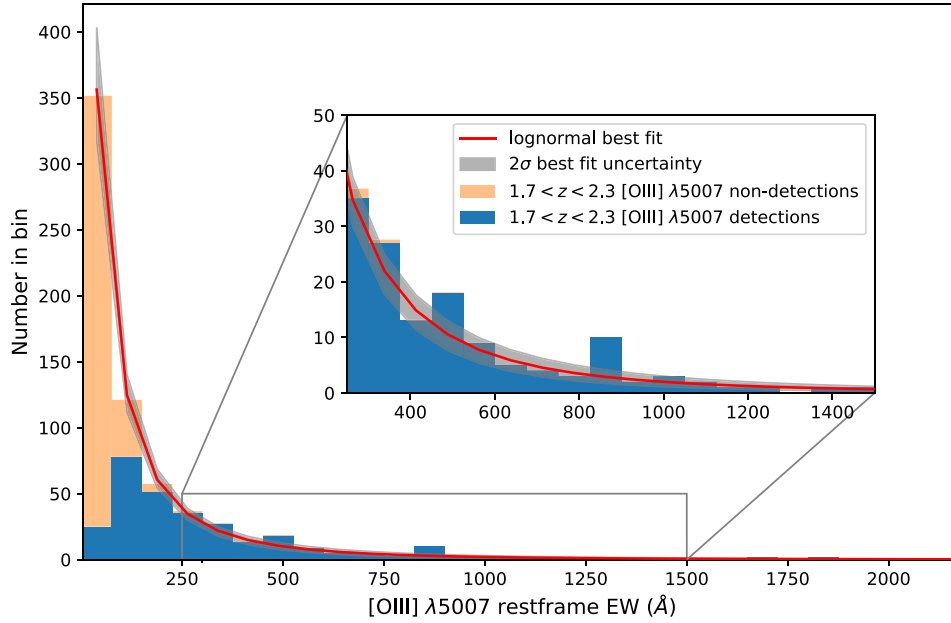


Figure 3. The EW distribution of [O III] λ 5007 for SFGs at $1.700 < z < 2.274$. The best-fitting lognormal model (red line) and 2σ uncertainties (grey), along with the EW histogram in 75 \AA bins for our M_{UV} selected sample constructed from 5σ [O III] doublet detections (blue) and 5σ upper limits (orange), where the histogram contribution from each [O III] doublet non-detection is assigned following the best-fitting model below the associated 5σ [O III] λ 5007 EW upper limit.

discussed above) and corrected to the rest-frame using the HDUV photometric redshifts.

Within our photometric sample, the sources with [O III] doublet detections in the grism spectra have rest-frame [O III] λ 5007 EWs ranging between 40 and 1800 \AA with a median of 214 \AA . For sources that are sufficiently bright in the continuum ($JH_{IR} < 23$), we are sensitive to low EWs ($< 50 \text{ \AA}$), allowing us to have a broad [O III] λ 5007 EW range, but for more typical magnitudes in our sample, the grism spectra are not sufficiently deep to reach such low [O III] λ 5007 EWs, and the line is undetected. For these, we find the median of the 5σ [O III] λ 5007 EW upper limits to be 93_{-4}^{+6} \AA , where we have additionally accounted for the effect of the uncertainty in the photometric redshifts on the EW upper limits.

The objects within our sample with large [O III] EWs are likely to have large specific star formation rates and sit above the SFR- M^* star-forming main sequence, as has been commonly seen in many EELG studies (e.g. Amorín et al. 2015; Onodera et al. 2020). The dynamic range of our sample’s NIR magnitudes means the distribution of EW measurements and upper limits overlap. A histogram of the resultant [O III] λ 5007 EWs is shown in Fig. 3. The detected sources (blue) are assigned to their appropriate EW bin while the contribution to the histogram from each EW upper limit source (orange) is spread over the EW parameter space below the 5σ upper limit, following the best-fitting lognormal distribution (discussed in Section 3.2). The sum of the probability across all bins below the 5σ upper limit equals 1 for an individual galaxy with no [O III] detection at 5σ .

3.2 Equivalent width distribution

As outlined in the introduction, our primary goal is to derive the [O III] λ 5007 EW distribution. In doing so we seek to quantify what proportion of the $z \sim 2$ population is in an extreme EW phase, as is believed to be common at $z > 7$. Equipped with robust measurements

and upper limits for the EW for our described sample, we can now characterize the distribution of EWs. We will model our sample, inclusive of non-detections, with a lognormal EW distribution. This functional form has been shown to be a good fit to other rest-optical EW samples (see Lee et al. 2007, 2012; Ly et al. 2011; Stark et al. 2013; Schenker et al. 2014; Endsley et al. 2021).

To infer the underlying [O III] λ 5007 EW distribution from our observed sample, we follow the Bayesian method set out by Schenker et al. (2014), which preserves information on each galaxy’s EW measurement uncertainty, while removing the need to bin the EW measurements. The EW distribution is modelled as a lognormal function $\theta = [\mu_{LN}, \sigma_{LN}]$.¹ We follow Schenker et al. (2014) and place a flat prior $P(\theta)$ over both the lognormal location μ_{LN} and variance σ_{LN} parameters, allowing the posterior to be determined directly as the model likelihood from our observed sample.

For a set of model parameters $[\mu_{\text{model}}, \sigma_{\text{model}}]$, the model lognormal probability distribution is given by

$$P(EW|\theta)_{\text{model}} = (2\pi \sigma_{\text{model}}^2 EW^2)^{-\frac{1}{2}} e^{-\frac{(\ln(EW) - \mu_{\text{model}})^2}{2\sigma_{\text{model}}^2}} \quad (1)$$

and the Gaussian measurement uncertainty on the measured EW is given by

$$P(EW)_{\text{obs}_i} = (2\pi \sigma_{\text{obs}_i}^2)^{-\frac{1}{2}} e^{-\frac{(EW - \mu_{\text{obs}_i})^2}{2\sigma_{\text{obs}_i}^2}} \quad (2)$$

Where μ_{obs_i} and σ_{obs_i} are the determined EW and observational uncertainty for the i^{th} system. The likelihood over the complete data set is taken as the product of the individual likelihoods of each galaxy

¹Equivalently this is the same as setting a normal distribution in logarithmic space with parameters $\theta = [\mu_N, \sigma_N]$. Both forms have been used in the literature and the relation between the normal distribution parameters and our lognormal parameters is given by; $\sigma_N = \sigma_{LN} \times \log_{10}(e)$ and $\mu_N = (\mu_{LN} - \sigma_{LN}^2) \times \log_{10}(e)$ and we will provide the best-fitting results from our analysis in both formats.

Table 1. Best-fitting model parameters for the rest-frame EW (\AA). We show the results for the lognormal distribution (LN) and normal distribution in logarithmic space (N).

Number	μ_{LN}	σ_{LN}	μ_{N}	σ_{N}
671	4.24 ± 0.07	1.33 ± 0.06	1.08 ± 0.10	0.58 ± 0.03

within the sample. The individual likelihood for each detected source (i) is defined as

$$P(\text{obs}_i|\theta)_{\text{detect}} = \int_0^\infty P(\text{EW})_{\text{obs}_i} \cdot P(\text{EW}|\theta)_{\text{model}} d\text{EW}. \quad (3)$$

The combination of the true EW distribution model with the Gaussian profile describing the EW measurement within the likelihood integral addresses observational noise to avoid overestimating the number of EELGs, where noise would preferentially scatter sources from the bulk of the distribution (with low EWs) towards extreme EW and broaden the observed EW distribution (up-scatter).

For sources which are undetected, the individual likelihood is defined by

$$P(\text{obs}_i|\theta)_{\text{non-detect}} = P(\text{EW} < \text{EW}_{5\sigma_i}|\theta) + P(\text{EW} > \text{EW}_{5\sigma_i}|\theta) \cdot C_{1,i} + C_2 \quad (4)$$

where $C_{1,i}$ is the proportion of the i^{th} spectra that is un-illuminated due to its location on the detector. C_2 is the photometric redshift in-scatter fraction, evaluated in Section 2.2 to be 4.4 per cent. This probability is determined as the sum of: the likelihood that the galaxy has a EW below the 5σ limit and the likelihood that the galaxy has an EW above this threshold multiplied by $C_{1,i}$ and C_2 . Due to the inclusion of the in-scatter term (C_2), this probability $P(\text{obs}_i|\theta)_{\text{non-detect}}$ may exceed 1 and so to avoid this a maximum value is enforced set equal to 1.

A Markov Chain Monte Carlo (MCMC) approach is taken to efficiently cover the parameter space using EMCEE (Foreman-Mackey et al. 2013). The marginalized posterior distributions over the lognormal parameters are used to determine the best-fitting model parameters, which are presented in Table 1. We over-plot the best-fitting model for the sample on the EW distribution in Fig. 3, with the 2σ model uncertainties indicated by the grey shaded region.

From our best-fitting results in Table 1, we report a mean (with standard error on the mean) and median EW of 168 ± 1 and $70 \pm 5 \text{\AA}$, with the EELG population skewing the mean EW higher than the median. This mean is within the expected [O III] λ 5007 EW range (80–250 \AA) for $\log_{10}(\frac{M}{M_\odot}) = 9 - 10$ stellar mass galaxies based on the $z \sim 2$ MOSDEF empirical relation by Reddy et al. (2018). The median is significantly lower than the $\sim 450 \text{\AA}$ median [O III] λ 5007 EW inferred for $z > 7$ samples (Labbé et al. 2013; De Barros et al. 2019; Endsley et al. 2021; when converted from [O III] + H β to [O III] λ 5007 EW assuming the assumptions detailed in Section 3.3). We note that the median [O III] λ 5007 EW in the sub-sample where the [O III] doublet is detected ($\geq 5\sigma$) was 214 \AA (see Section 3.1), whereas now by modelling the whole sample including those galaxies with [O III] non-detections through our Bayesian analysis, we determine a best-fitting EW distribution model that has a lower median [O III] λ 5007 EW of 70 \AA . This should be expected since intrinsically low EW sources would be more likely to have [O III] doublet non-detections.

Through fitting a functional form, the proportion of SFGs with an EW above a given threshold can be easily calculated and we shall call this the EELG fraction. For each set of model parameters θ of the MCMC run, the EELG fraction is recorded and the resultant posterior

density function (PDF) over all models is then used to estimate the best-fitting overall EELG fraction and uncertainty for the population (see Fig. 4, discussed below).

Within the literature, there is no set definition for the threshold [O III] λ 5007 EW a galaxy must have to be classified as an EELG and the quoted threshold varies from author to author. Commonly taken threshold values range from [O III] λ 5007 EW ~ 100 – 1000\AA . At low redshift, Amorín et al. (2015) employ a $\geq 100 \text{\AA}$ threshold to construct an EELG subset from a $0.11 < z < 0.93$ SFG sample, and in our distribution this EW threshold results in an EELG fraction of 39_{-3}^{+2} per cent at $z \sim 2$. At intermediate redshifts, considerable attention has been focused on photometric selection of EELGs, for example, van der Wel et al. (2011) who identify $z \sim 1.7$ galaxies through *HST* J-band (F125W) flux excess. These selected EELGs at $z \sim 1.7$ tend to have [O III] λ 5007 EWs above 500 \AA , which is comparable to the typical [O III] λ 5007 EW found at $z > 7$. Adopting a threshold of 500 \AA yields an EELG fraction of $6.8_{-0.9}^{+1.0}$ per cent in our EW distribution at $z \sim 2$.

More recently, spectroscopic work at $z \sim 2$ exploring the stellar population and gas properties as a function of [O III] λ 5007 EW (e.g. Tang et al. 2019, 2021a; Du et al. 2020) has focused on the most extreme line emitters, those with [O III] λ 5007 EWs above 750 or 1000 \AA . These are the galaxies at $z \sim 2$ found to have the highest ξ_{ion} , O32 values, and the potential for large ionizing escape fractions. In our $z \sim 2$ distribution these are rare, accounting for only $3.6_{-0.6}^{+0.7}$ per cent above a threshold of 750 \AA and $2.2_{-0.4}^{+0.5}$ per cent above a threshold of 1000 \AA .

In Fig. 4, we present the EELG fraction PDF for four [O III] λ 5007 EW thresholds. These correspond to the rough mean [O III] λ 5007 EW of SFGs at $z \sim 2$ (200 \AA), the typically EW of SFGs at $z > 7$ (500 \AA) and the EW seen in the most extreme line emitters at $z \sim 2$ (750 and 1000 \AA). The 200 \AA threshold accounts for roughly a fifth of SFGs at $z \sim 2$ with the higher EW thresholds recovering diminishing fractions. The 500 \AA threshold highlights that the SFGs common at $z > 7$ are rare at $z \sim 2$, with the most extreme candidates effectively absent from the $z \sim 2$ population. We present the measured EELG fractions for each [O III] λ 5007 EW threshold in Table 2.

3.3 Redshift evolution of the EELG fraction

The [O III] λ 5007 EW distribution produced in the previous section provides a baseline to probe the redshift evolution of EELGs from $z \sim 2$ out into the EOR. Our best-fitting distribution for $z \sim 2$ SFGs produces a mean and a median EW of 168 \AA and 70 \AA , whereas recent work at $z > 7$ show a median EW of $\sim 450 \text{\AA}$ (Labbé et al. 2013; De Barros et al. 2019; Endsley et al. 2021), suggesting significant evolution in the typical EW in the two billion years between these two epochs. This trend likely reflects evolution in the sSFR and metallicity. In what follows, we seek to use our EW distribution to quantify the redshift evolution in the fraction of EELGs, using the various EW thresholds as discussed in the Section 3.2.

We will compare our $z \sim 2$ measurements to studies of galaxies at higher redshift which also select on rest-frame UV luminosity. We consider three higher redshift studies that characterize rest-optical EW distributions: Stark et al. (2013) at $z \sim 4 - 5$; Rasappu et al. (2016) at $z \sim 5$; and Endsley et al. (2021) at $z \sim 7$. These three studies are all based on *Spitzer*/IRAC colours of Lyman break galaxies, where the flux excess between two adjacent filters is attributed to the presence of strong nebular lines (either [O III] λ 4959, 5007 + H β or H α depending on the redshift and filter) allowing the rest-optical nebular EWs to be measured for samples of SFGs. Our primary comparison will be to Endsley et al. (2021) who model

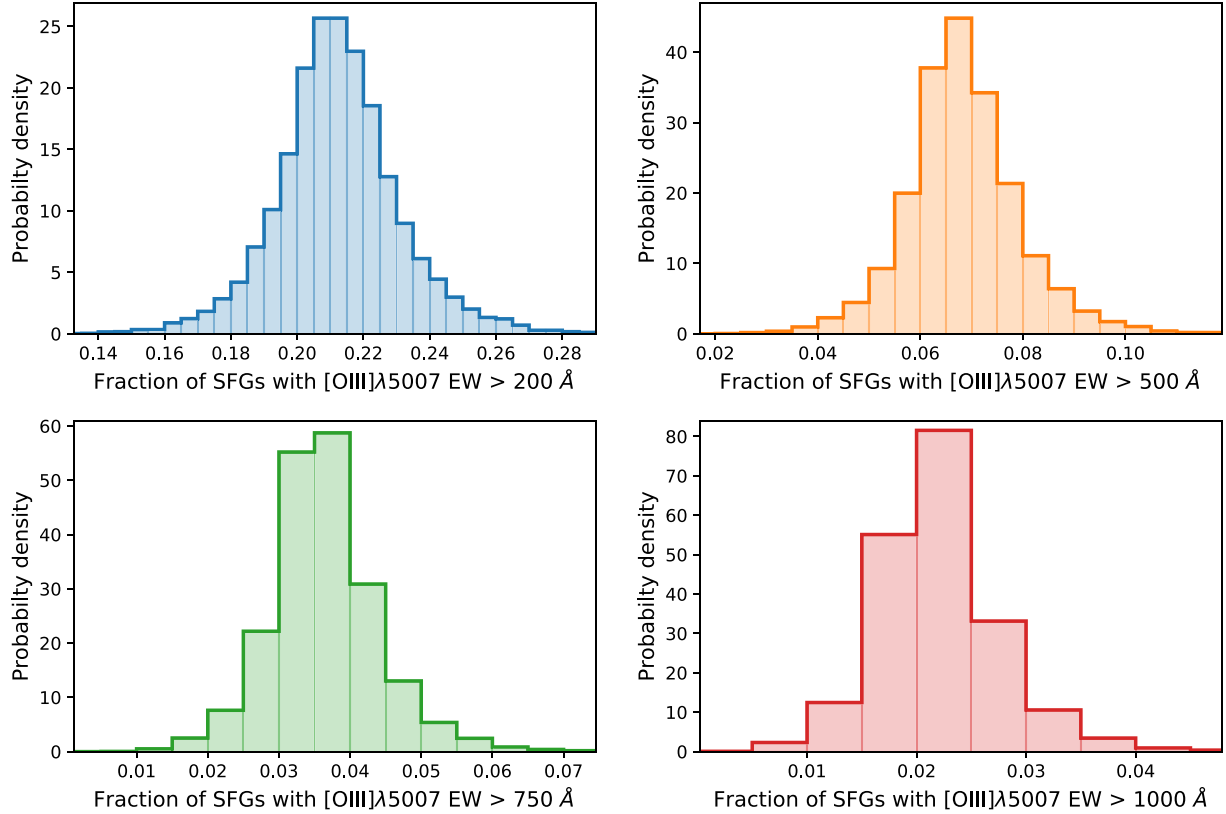


Figure 4. The fraction of SFGs at $z \sim 2$ with extremely large [O III] λ 5007 EW. Posterior distributions for four different [O III] λ 5007 EW thresholds are shown in blue (200 Å, top-left panel), orange (500 Å, top-right panel), green (750 Å, bottom-left panel), and red (1000 Å, bottom-right panel).

Table 2. The fraction of SFGs in an extreme emission line phase (the EELG fraction) with [O III] λ 5007 EW above four rest-frame EW thresholds. The EELG fractions are presented as a percentage (%) for the full $z \sim 2$ UV-selected sample, the sample split into two redshift bins and the sample split into two bins of UV luminosity.

Sample	EW \geq 200 Å	EW \geq 500 Å	EW \geq 750 Å	EW \geq 1000 Å
Full sample	21.2 $^{+1.7}_{-1.6}$ %	6.8 $^{+1.0}_{-0.9}$ %	3.6 $^{+0.7}_{-0.6}$ %	2.2 $^{+0.5}_{-0.4}$ %
1.70 < z < 2.01	19.7 $^{+2.1}_{-2.1}$ %	5.4 $^{+1.2}_{-1.1}$ %	2.6 $^{+0.8}_{-0.9}$ %	1.5 $^{+0.6}_{-0.4}$ %
2.01 < z < 2.274	22.8 $^{+2.6}_{-2.3}$ %	8.2 $^{+1.6}_{-1.5}$ %	4.7 $^{+1.2}_{-1.1}$ %	3.0 $^{+0.9}_{-0.8}$ %
-19.5 < M_{UV} < -19	20.1 $^{+2.4}_{-2.1}$ %	6.7 $^{+1.4}_{-1.3}$ %	3.6 $^{+1.0}_{-0.9}$ %	2.3 $^{+0.8}_{-0.7}$ %
-21.6 < M_{UV} < -19.5	22.3 $^{+2.4}_{-2.3}$ %	7.1 $^{+1.5}_{-1.3}$ %	3.7 $^{+1.0}_{-0.8}$ %	2.2 $^{+0.7}_{-0.6}$ %

the [O III] λ 4959, 5007 + $H\beta$ EW distribution from 22 Lyman break dropouts at $6.63 < z < 6.83$. To compare against EELG fractions from Endsley et al. (2021), we scale the [O III] λ 5007 EW thresholds into appropriate [O III] λ 4959, 5007 + $H\beta$ thresholds. As described previously, we obtain the [O III] λ 4959, 5007 threshold through a 2.98:1 flux ratio between [O III] λ 5007 and [O III] λ 4959 (Storey & Zeippen 2000). For $H\beta$, we infer the EW contribution using an $H\beta$: [O III] λ 5007 EW empirical relation ($\log_{10}(H\beta \text{ EW}) = 1.065 \times \log_{10}([O III]\lambda 5007 \text{ EW}) - 0.938$) obtained from the Tang et al. (2019) results for a comparable sample of $1.3 < z < 2.4$ EELGs covering a sufficiently broad [O III] λ 5007 EW range (~ 100 – 2500 Å). Here, our 500, 750, and 1000 Å [O III] λ 5007 EW thresholds are equivalent to 754, 1135, and 1516 Å [O III]+ $H\beta$ EW thresholds. Our comparison sample also includes two $H\alpha$ EW studies: Stark et al. (2013) at $3.8 < z < 5$; and Rasappu et al. (2016) at $5.1 < z < 5.4$. In order to convert our

[O III] λ 5007 EW thresholds into that appropriate for the $H\alpha$ studies, we apply a conversion factor from the linear relation found by Tang et al. (2019) between $H\alpha$ and [O III] λ 5007 EW in EELGs. A scaling factor $\text{EW}(H\alpha)/\text{EW}([O III]\lambda 5007) = 1.0$ for [O III] λ 5007 between 450 and 800 Å and 1.1 between 800 and 2500 Å. This mapping suggests that our 500, 750, and 1000 Å [O III] λ 5007 EW thresholds are roughly equivalent to 500, 750, and 1100 Å $H\alpha$ EW thresholds. These conversions are comparable to what has been used in the literature previously (e.g. Labbé et al. 2013; Rasappu et al. 2016).

To characterize the redshift evolution within our data set, we divide our $z \sim 2$ sample into two redshift bins, $1.70 \leq z \leq 2.01$ and $2.01 < z \leq 2.274$ containing 328 and 343 galaxies, respectively (using spectroscopic redshifts for [O III] doublet detections and photometric redshifts for non-detections). We report EELG fractions for the two redshift bins in Table 2 and the full set of best-fitting parameters for both sub-samples in Table 3. Fig. 5 shows the EELG

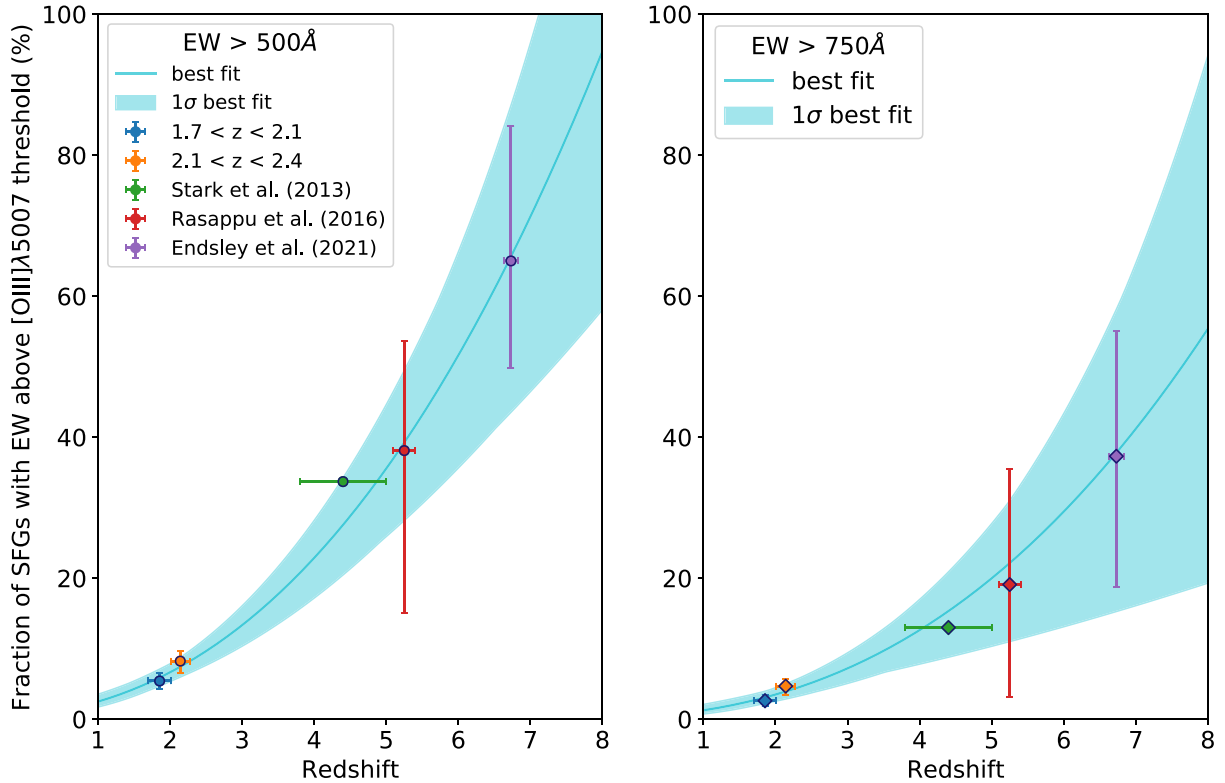


Figure 5. The evolution of the fraction of SFGs with extremely large [O III] λ 5007 EW. The fraction for two [O III] λ 5007 EW thresholds shown in circles (left plot – 500 Å) and diamonds (right plot – 750 Å) across five redshift epochs shown in blue ($1.70 < z < 2.01$), orange ($2.01 < z < 2.274$), green ($3.8 < z < 5.0$), red ($5.1 < z < 5.4$), and purple ($6.63 < z < 6.83$). Our $z \sim 2$ data points are compared to the $H\alpha$ studies at $z \sim 5$ and the [O III] + $H\beta$ study at $z \sim 7$ assuming conversions to [O III] λ 5007 EW. A fitted power-law slope $\propto (1+z)^P$ and associated 1σ uncertainty are shown in light blue.

fractions calculated at [O III] λ 5007 EW thresholds of 500 and 750 Å and compares to results in the literature at higher redshift.

It is clear from Fig. 5 that at higher redshifts a greater proportion of SFGs are observed in an extreme emission line phase. Not only are the typical SFGs at $z \sim 7$ ([O III] λ 5007 EW ~ 500 Å) rare at $z \sim 2$, representing $5.4^{+1.2}_{-1.1}$ per cent and $8.2^{+1.6}_{-1.5}$ per cent of the population in our $1.70 < z < 2.01$ and $2.01 < z < 2.274$ bins, but conversely the SFGs typical of $z \sim 2$ ([O III] λ 5007 EW ≤ 200 Å) are rare at $z \sim 7$, making up only ~ 3 per cent of SFGs at these high redshifts (Endsley et al. 2021). It has been argued that objects with [O III] λ 5007 EW above 1000 Å lie above the star-forming main sequence (the relation between the SFR of a galaxy and the stellar mass, see e.g. Speagle et al. 2014). Such intense line emitters encompass ~ 20 per cent of the population at $z > 7$, but at $z \sim 2$ these objects are practically insignificant, with only $1.5^{+0.6}_{-0.4}$ per cent ($1.70 < z < 2.01$) and $3.0^{+0.9}_{-0.8}$ per cent ($2.01 < z < 2.274$) of SFGs in such a phase in our two intermediate redshift bins. We consider a power-law fit to the redshift evolution of the EELG fraction ($\text{frac}(z) = \text{frac}_0 (1+z)^P$) and find $z = 0$ fraction and power-law slope parameters ($\text{frac}_0 = 0.47^{+0.12}_{-0.10}$ per cent, $P = 2.42^{+0.18}_{-0.18}$) for an EW threshold of 500 Å and ($\text{frac}_0 = 0.22^{+0.11}_{-0.07}$ per cent, $P = 2.51^{+0.27}_{-0.32}$) for an EW thresholds of 750 Å.

3.4 The dependence of the EELG fraction on UV luminosity

Here, we characterize the luminosity-dependence of the [O III] λ 5007 EW distribution in the range sampled by our data set ($-21.6 < M_{\text{UV}} < -19$). At $z \sim 7$, an analysis using *Spitzer*/IRAC flux excesses as a probe of rest-optical line strengths found no evidence for

Table 3. Best-fitting model parameters for the rest-frame EW(Å). We show the results for the lognormal distribution (LN) and normal distribution in logarithmic space (N) for our two redshift sub-samples.

z-range	N	μ_{LN}	σ_{LN}	μ_{N}	σ_{N}
1.70 – 2.01	328	$4.26^{+0.09}_{-0.09}$	$1.21^{+0.08}_{-0.07}$	$1.21^{+0.12}_{-0.11}$	$0.53^{+0.03}_{-0.03}$
2.01 – 2.274	343	$4.26^{+0.11}_{-0.12}$	$1.43^{+0.11}_{-0.10}$	$0.97^{+0.18}_{-0.18}$	$0.62^{+0.05}_{-0.04}$

a significant [O III] + $H\beta$ EW trend with M_{UV} (Endsley et al. 2021). Given the close connection between [O III] λ 5007 EW and the ionizing efficiency (see discussion in Section 1), this result has implications for the M_{UV} -dependent contribution of galaxies to reionization. Physically, we may expect the [O III] λ 5007 EW to be stronger towards lower UV luminosities given the correlation between M_{UV} and stellar mass at $z \sim 2$ (e.g. Reddy & Steidel 2009) and the relationship between mass and metallicity (e.g. Sanders et al. 2021). The larger electron temperature in lower metallicity systems can act to boost collisionally excited emission lines such as [O III] λ 5007 (Reddy et al. 2018). The [O III] λ 5007 EW additionally depends on the sSFR (e.g. Tang et al. 2019). This is especially true at very large sSFR, where the [O III] λ 5007 EW is enhanced by the weak underlying rest-optical continuum associated with very young stellar populations. If the large sSFR phase is more common in galaxies with lower UV luminosities (as might be expected if bursts are more common in lower luminosity and lower mass systems), we would expect to see larger EELG fractions at the faint end of the luminosity function.

Table 4. Best-fitting model parameters for the rest-frame EW(Å). We show the results for the lognormal distribution (LN) and normal distribution in logarithmic space (N) for our two M_{UV} sub-samples.

M_{UV}	N	μ_{LN}	σ_{LN}	μ_N	σ_N
−19.5 to −19.0	335	$4.13^{+0.12}_{-0.12}$	$1.39^{+0.12}_{-0.11}$	$0.95^{+0.19}_{-0.18}$	$0.60^{+0.05}_{-0.05}$
−21.6 to −19.5	336	$4.31^{+0.08}_{-0.09}$	$1.30^{+0.08}_{-0.07}$	$1.14^{+0.13}_{-0.12}$	$0.57^{+0.03}_{-0.03}$

To investigate whether the [O III]λ5007 EW distribution varies with UV luminosity, we first separate our sample into a UV-bright ($-21.6 < M_{UV} < -19.5$, 336 galaxies) and UV-faint sub-sample ($-19.5 < M_{UV} < -19$, 335 galaxies). We recompute the best-fitting lognormal parameters for the [O III]λ5007 EW distributions in both magnitude bins. The results reveal broad consistency in the model mean and also the median of the two M_{UV} bins: the mean EW values of the UV-faint and UV-bright samples are $165.1^{+2.0}_{-1.5}$ and $174^{+1.4}_{-1.1}$ Å, respectively (where we quote the standard error on the mean), and the median values are 63^{+8}_{-7} and 74^{+7}_{-6} Å. The full set of best-fitting parameters for both sub-samples is presented in Table 4. As can be seen in the Table, both the average and width of the EW distributions are consistent within 2σ .

We also consider the luminosity-dependence of the EELG population, computing the fraction of galaxies that have [O III]λ5007 EWs above four physically motivated thresholds (200, 500, 750, and 1000 Å, see Table 2). The EELG fraction PDFs for both UV bins are shown in Fig. 6. For each threshold (each sub-panel in Fig. 6) the derived fraction of SFGs with an [O III]λ5007 EW above the given threshold is consistent between the two luminosity sub-samples. The fraction of galaxies with an EW above the typical [O III]λ5007 EW at $z \simeq 2$ (200 Å) is similar in the fainter and brighter bins (from $20.1^{+2.4}_{-2.1}$ per cent to $22.3^{+2.4}_{-2.3}$ per cent), and the same is found for the relative abundance of the most EELGs ($EW \geq 1000$ Å) ($2.3^{+0.8}_{-0.7}$ per cent and $2.2^{+0.7}_{-0.6}$ per cent for the fainter and brighter bins). The absence of significant variations in the [O III]λ5007 EW distributions between the UV-bright and UV-faint bins is consistent with the findings of Endsley et al. (2021) at $z \simeq 7$. A larger dynamic range in M_{UV} may be required to find a trend between [O III]λ5007 EW and UV luminosity.

4 DISCUSSION

In this paper, we have derived the [O III]λ5007 EW distribution in $z \simeq 2$ UV-selected galaxies, thereby quantifying the fraction of EELGs at $z \simeq 2$. Locally ($z \sim 0$) and at intermediate redshifts ($1 < z < 3$), EELGs have been shown to be extremely efficient ionizers, both due to their large ionization production efficiencies (Chevallard et al. 2018; Tang et al. 2019; Emami et al. 2020; Nakajima et al. 2020) and their large escape fractions (e.g. Izotov et al. 2016; Vanzella et al. 2016; Fletcher et al. 2019; Jaskot et al. 2019; Nakajima et al. 2020). However, the rareness of this population suggests they are likely to make a sub-dominant contribution to the ionizing background from SFGs at $z \simeq 2$. In this section, we estimate the fractional contribution from EELGs at $z \simeq 2$ to the ionizing background, combining [O III]λ5007 EW distributions with nominal assumptions on the ionizing efficiency of the population.

We first consider the ionizing contribution of EELGs at $z \simeq 2$, focusing on those systems with [O III]λ5007 EW > 750 Å. While this subset comprises just 3.6 per cent of the $z \simeq 2$ population (Table 2), they are thought to be very efficient ionizers. These objects have typical ionizing photon production efficiencies of $\log_{10}(\xi_{ion}, \text{erg s}^{-1}\text{Mpc}^{-3}\text{Hz}^{-1}) = 25.58$ (Tang et al. 2019), $3.3\times$ greater than that

in more typical SFGs at $z \simeq 2$ (Shivaei et al. 2018). While not all EELGs show ionizing photon leakage, values are often significant in the population, with systems having the largest [O III]λ5007 EWs (i.e. > 750 Å) often found with estimated escape fractions of up to 20–50 per cent (Vanzella et al. 2016; Rivera-Thorsen et al. 2017; Izotov et al. 2018; Fletcher et al. 2019). For the purposes of this calculation, we will assume that this range of 20 – 50 per cent escape fractions is exhibited by half of galaxies with [O III]λ5007 EW > 750 Å, with the remaining half leaking no ionizing radiation. While this f_{esc} distribution is clearly still very uncertain, the values are broadly consistent with known constraints on LyC escape fractions and indirect indicators of leakage in this extreme [O III] emitting population (e.g. Izotov et al. 2018; Jaskot et al. 2019; Du et al. 2020; Tang et al. 2021b). In what follows, we take these values and calculate the comoving emissivity of ionizing photons ($\dot{n}_{ion}, \text{s}^{-1}\text{Mpc}^{-3}$) for these intense EELGs, but we caution that improved distributions of escape fractions in this population are ultimately required for more confident inferences. We focus on galaxies in the luminosity range probed in this paper ($-21.6 < M_{UV} < -19$) and assume the Reddy & Steidel (2009) UV luminosity function. We multiply the far-UV luminosity density by the fraction of galaxies with [O III]λ5007 EW > 750 Å (3.6 per cent). After accounting for the ionizing production efficiency and the range of escape fractions, we find that this population injects a comoving ionizing photon emissivity of between 3 and $8 \times 10^{49} \text{ s}^{-1} \text{ Mpc}^{-3}$ into the IGM at $z \simeq 2$ for our assumed parameters. We can now estimate the fractional contribution these EELGs make to the total ionizing background produced by $z \simeq 2$ SFGs. To do so, we use population-average estimates of the ionizing photon production efficiency and escape fraction. For the escape fraction, we use the recently derived value from Pahl et al. (2021), indicating an average f_{esc} of ~ 6 per cent for $z \simeq 3$ UV-selected galaxies, consistent with the latest determination of 7 ± 2 per cent from the VANDELS survey Begley et al. (2022). We adopt this value of 6 per cent from Pahl et al. (2021) but we note that there is variation in the measurements of f_{esc} at $z > \sim 3$ in the literature; Steidel et al. (2018) report 9 ± 1 per cent, while Grazian et al. (2017) place an upper limit of $f_{esc} < 10$ per cent for a stack of $z \sim 3$ galaxies with $M_{UV} \approx -19.7$ (close to the median M_{UV} of our sample in this paper). Here, we assume that $z \simeq 2$ galaxies have a similar value. For the ionizing production efficiency, we use the value derived for the $z \simeq 2$ UV-selected population, taking the same attenuation law as we assumed for EELGs (Shivaei et al. 2018). The estimated ionizing emissivity from UV-selected galaxies over our luminosity range is then $\dot{n}_{ion} = 1.5 \times 10^{50} \text{ s}^{-1}\text{Mpc}^{-3}$. While the emissivities quoted above are nominal estimates with significant uncertainties, they illustrate that EELGs do indeed make a sub-dominant contribution to ionizing output from galaxies at $z \simeq 2$ (accounting for 20–50 per cent of the ionizing flux from all SFGs). However if the large escape fractions assumed here for a subset of the most intense of EELGs are correct, it would indicate that even at $z \simeq 2$, this population makes a non-negligible contribution to the ionizing background of SFGs.

The ionizing contribution from EELGs is likely to increase substantially as we enter the reionization era. Given current constraints on the $z \simeq 7$ [O III] + H β EW distribution from Endsley et al. (2021) and nominal assumptions about the relation between [O III] + H β and [O III]λ5007 EWs (see Section 3.3), the percentage of SFGs with [O III]λ5007 EW > 750 Å increases by a factor of 10 between $z \simeq 2$ and $z \simeq 7$, from 3.6 per cent ($z \simeq 2$) to close to 37 per cent ($z \simeq 7$). The percentage of those with an [O III]λ5007 EW > 500 Å also increases by a factor of 10 between $z \sim 2 - 7$, reaching close to 65 per cent of the population at $z \simeq 7$ (Endsley et al. 2021). So

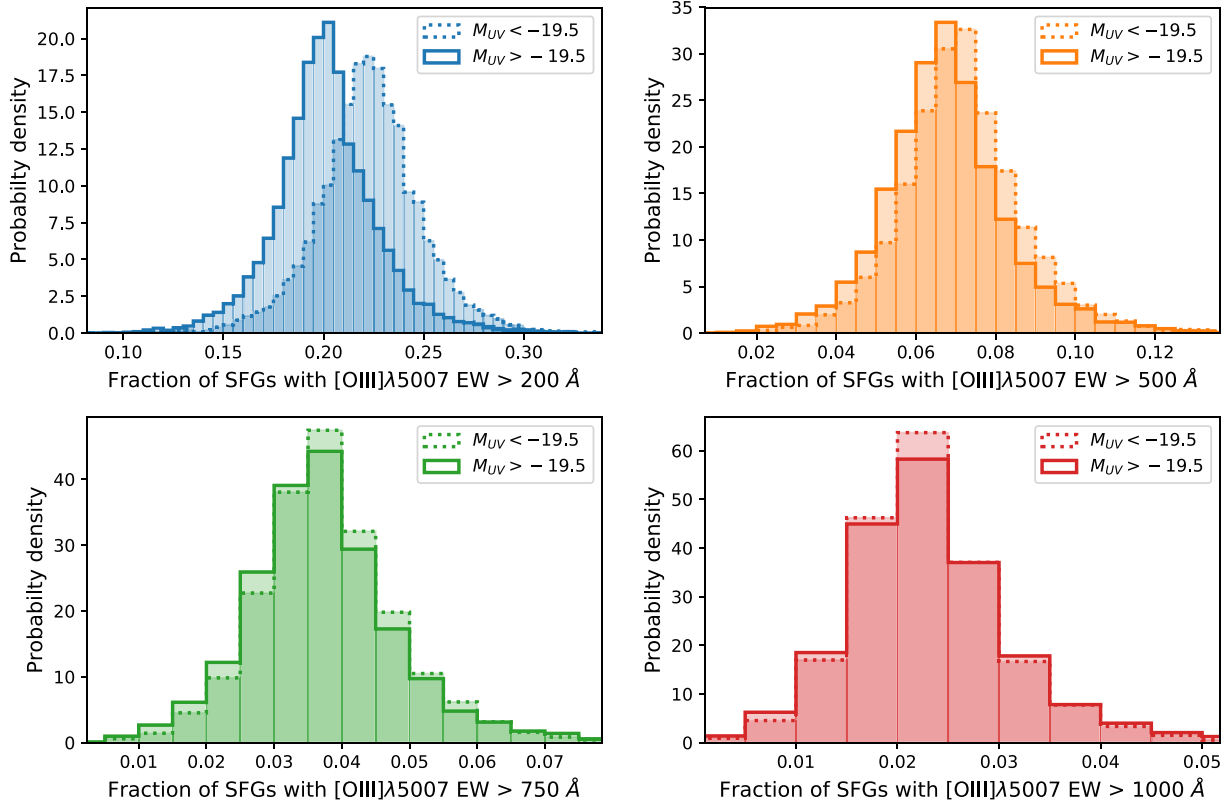


Figure 6. The fraction of M_{UV} bright and M_{UV} faint SFGs at $z \sim 2$ with extremely large [O III] λ 5007 EW. Posterior distributions for the bright $-21.6 < M_{UV} < -19.5$ (solid lines) and faint $-19.5 < M_{UV} < -19.0$ (dashed lines) shown for four different [O III] λ 5007 EW thresholds in blue (200 Å), orange (500 Å), green (750 Å), and red (1000 Å).

while the majority of the $z \sim 2$ SFG ionizing background comes from more typical modes of star formation than EELGs, during the reionization era the bulk of the ionizing photons will likely come from EELGs. Future work is required to test if the ionizing efficiency of this population evolves with redshift. The first spectra of EELGs in the reionization era suggest similarly intense radiation fields as are often seen at lower redshifts (e.g. Stark et al. 2015a, b, 2017; Mainali et al. 2017; Schmidt et al. 2017; Hutchison et al. 2019; Jiang et al. 2021; Topping et al. 2021), but *JWST* will soon allow much-improved investigation of the ionizing output of reionization-era EELGs.

The rapid evolution in the EELG population is suggestive of a shift in the main star-forming mode between $z \sim 2$ and $z \sim 7$. The most intense EELGs are likely in the midst of a burst or recent upturn in star formation. The increase in this population with redshift may suggest that such intense bursts are becoming more common in the reionization era. This is perhaps consistent with the observed rise in the galaxy merger rate and specific mass accretion rate observed between $1 < z < 6$ (Duncan et al. 2019), both of which may spark and feed more frequent and stronger bursts of star formation. The nebular rest-optical line EW distributions (and the related sSFR distributions) encode useful information on the star formation history, with the tails of the distribution (both at high and low sSFR) constraining the strength and duty cycle of bursts. The evolution and mass-dependence of these distributions will soon be constrained in more detail by *JWST*. Direct comparison of these observations to simulations and semi-analytic models promises valuable insight into the presence of bursts in the earliest galaxies.

5 SUMMARY

Recent years have seen increased interest in EELGs, owing to their efficiency as ionizing agents and their apparent ubiquity in the reionization era. The [O III] λ 5007 EW distribution constrains the percentage of SFGs at a given epoch caught in an extreme emission line phase. While efforts have begun to characterize the distribution of [O III] + H β line strengths at $z \simeq 7$ (Labbé et al. 2013; Smit et al. 2014; De Barros et al. 2019; Endsley et al. 2021), similar measurements do not exist at $z \simeq 2$, impeding efforts to track the redshift evolution of the EELG population. We establish the best-fitting lognormal model for the [O III] λ 5007 EW distribution in a rest-UV selected sample ($M_{UV} < -19$) in the redshift range $1.700 < z < 2.274$, using the combination of HDUV photometry and the 3D-*HST* grism spectra. With the [O III] λ 5007 EW distribution, we quantify the fraction of $z \simeq 2$ galaxies with extreme line emission, providing the low redshift baseline necessary to characterize the evolution of this population. The fraction of UV-selected galaxies with an [O III] λ 5007 EW above 200, 500, 750, and 1000 Å is found to be $21.2^{+1.7}_{-1.6}$ per cent, $6.8^{+1.0}_{-0.9}$ per cent, $3.76^{+0.7}_{-0.6}$ per cent, and $2.2^{+0.5}_{-0.4}$ per cent, respectively. We find no strong evidence that the EELG fractions vary with UV luminosity in the range considered in this paper ($-21.6 < M_{UV} < -19.0$), consistent with results at $z \simeq 7$ (Endsley et al. 2021).

Comparison to results at higher redshift (e.g. De Barros et al. 2019; Endsley et al. 2021) reveals rapid redshift evolution, with the fraction of galaxies having [O III] λ 5007 EW > 500 Å increasing from 6.8 per cent at $z \simeq 2$ to 65 per cent at $z \simeq 7$ (for nominal assumptions about the H β contribution at $z \simeq 7$). We find a similar increase

with a slightly higher [O III] λ 5007 EW threshold ($>750 \text{ \AA}$), with 3.6 per cent of the population in this regime at $z \simeq 2$ and 37 per cent at $z \simeq 7$. Even accounting for their enhanced ionizing efficiency, EELGs are too rare at $z \sim 2$ to dominate the ionizing background produced by SFGs. However, a far greater percentage of galaxies will be in an extreme emission line phase at $z \simeq 7$, providing an ideal population for ionizing the IGM. Future work will soon offer much-improved measures of the evolving EELG population, both in terms of their ionizing efficiency and their mass-dependent contribution to the total galaxy population. These studies promise valuable insights into the contribution of galaxies to reionization and the redshift and mass-dependence of bursts in early galaxies.

ACKNOWLEDGEMENTS

KB acknowledges funding from the Science and Technology Facilities Council (STFC) Grant Code ST/R505006/1. AJB has received funding from the European Research Council (ERC) under the European Union's Horizon 2020 Advanced Grant 789056 'First Galaxies'. This work is based on observations taken by the 3D-*HST* Treasury Program (*HST*-GO-12177 and *HST*-GO-12328) with the NASA/ESA *Hubble Space Telescope*, which is operated by the Association of Universities for Research in Astronomy, Inc., under NASA contract NAS5-26555. This research was supported by the Australian Research Council Centre of Excellence for All Sky Astrophysics in 3 Dimensions (ASTRO 3D) through project CE170100013.

DATA AVAILABILITY

This work is based on public data available from the *HST* archive, and we have used the data products released by 3D-*HST* and HDUV. The catalogues and analysis routines used in this work are available upon reasonable request to the authors.

REFERENCES

- Alexander D. M. et al., 2003, *AJ*, 126, 539
 Amorín R. O., Pérez-Montero E., Vílchez J. M., 2010, *ApJ*, 715, L128
 Amorín R. et al., 2015, *A&A*, 578, A105
 Atek H. et al., 2010, *ApJ*, 723, 104
 Atek H. et al., 2011, *ApJ*, 743, 121
 Balestra I. et al., 2010, *A&A*, 512, A12
 Barro G. et al., 2019, *ApJS*, 243, 22
 Bassett R. et al., 2019, *MNRAS*, 483, 5223
 Begley R. et al., 2022, preprint ([arXiv:2202.04088](https://arxiv.org/abs/2202.04088))
 Bouwens R. J., Illingworth G. D., Oesch P. A., 2015a, *ApJ*, 803, 34
 Bouwens R. J., Illingworth G. D., Oesch P. A., Caruana J., Holwerda B., Smit R., Wilkins S., 2015b, *ApJ*, 811, 140
 Boylan-Kolchin M., 2018, *MNRAS*, 479, 332
 Brammer G. B., van Dokkum P. G., Coppi P., 2008, *ApJ*, 686, 1503
 Brammer G. B. et al., 2012, *ApJS*, 200, 13
 Brunner S. W., Salzer J. J., Janowiecki S., Finn R. A., Helou G., 2020, *ApJ*, 898, 68
 Bunker A. J., Stanway E. R., Ellis R. S., McMahon R. G., 2004, *MNRAS*, 355, 374
 Bunker A. J. et al., 2010, *MNRAS*, 409, 855
 Cardamone C. et al., 2009, *MNRAS*, 399, 1191
 Castellano M. et al., 2017, *ApJ*, 839, 73
 Chevallard J. et al., 2018, *MNRAS*, 479, 3264
 De Barros S., Oesch P. A., Labbé I., Stefanon M., González V., Smit R., Bouwens R. J., Illingworth G. D., 2019, *MNRAS*, 489, 2355
 Du X., Shapley A. E., Tang M., Stark D. P., Martin C. L., Mobasher B., Topping M. W., Chevallard J., 2020, *ApJ*, 890, 65
 Duncan K. et al., 2019, *ApJ*, 876, 110
 Emami N., Siana B., Alavi A., Gburek T., Freeman W. R., Richard J., Weisz D. R., Stark D. P., 2020, *ApJ*, 895, 116
 Endsley R., Stark D. P., Chevallard J., Charlot S., 2021, *MNRAS*, 500, 5229
 Eyles L. P., Bunker A. J., Stanway E. R., Lacy M., Ellis R. S., Doherty M., 2005, *MNRAS*, 364, 443
 Eyles L. P., Bunker A. J., Ellis R. S., Lacy M., Stanway E. R., Stark D. P., Chiu K., 2007, *MNRAS*, 374, 910
 Finkelstein S. L., Ryan R. E. Jr, Papovich C., 2015, *ApJ*, 810, 71
 Finkelstein S. L. et al., 2019, *ApJ*, 879, 36
 Fletcher T. J., Tang M., Robertson B. E., Nakajima K., Ellis R. S., Stark D. P., Inoue A., 2019, *ApJ*, 878, 87
 Foreman-Mackey D., Hogg D. W., Lang D., Goodman J., 2013, *PASP*, 125, 306
 Fumagalli M. et al., 2012, *ApJ*, 757, L22
 Garilli B. et al., 2021, *A&A*, 647, A150
 Grazian A. et al., 2017, *A&A*, 602, A18
 Hutchison T. A. et al., 2019, *ApJ*, 879, 70
 Inami H. et al., 2017, *A&A*, 608, A2
 Izotov Y. I., Guseva N. G., Thuan T. X., 2011, *ApJ*, 728, 161
 Izotov Y. I., Schaerer D., Thuan T. X., Worseck G., Guseva N. G., Orlitová I., Verhamme A., 2016, *MNRAS*, 461, 3683
 Izotov Y. I., Worseck G., Schaerer D., Guseva N. G., Thuan T. X., Fricke Verhamme A., Orlitová I., 2018, *MNRAS*, 478, 4851
 Jaskot A. E., Dowd T., Oey M. S., Scarlata C., McKinney J., 2019, *ApJ*, 885, 96
 Jiang L. et al., 2021, *Nature Astron.*, 5, 256
 Kurk J. et al., 2013, *A&A*, 549, A63
 Labbé I. et al., 2013, *ApJ*, 777, L19
 Laporte N., Nakajima K., Ellis R. S., Zitrin A., Stark D. P., Mainali R., Roberts-Borsani G. W., 2017, *ApJ*, 851, 40
 Le Fèvre O. et al., 2005, *A&A*, 439, 845
 Le Fèvre O. et al., 2015, *A&A*, 576, A79
 Lee J. C., Kennicutt R. C., Funes S. J. J. G., Sakai S., Akiyama S., 2007, *ApJ*, 671, L113
 Lee J. C. et al., 2012, *PASP*, 124, 782
 Luo B. et al., 2017, *ApJS*, 228, 2
 Ly C., Lee J. C., Dale D. A., Momcheva I., Salim S., Staudaher S., Moore C. A., Finn R., 2011, *ApJ*, 726, 109
 Madau P., Haardt F., 2015, *ApJ*, 813, L8
 Mainali R., Kollmeier J. A., Stark D. P., Simcoe R. A., Walth G., Newman A. B., Miller D. R., 2017, *ApJ*, 836, L14
 Mainali R. et al., 2018, *MNRAS*, 479, 1180
 Maseda M. V. et al., 2014, *ApJ*, 791, 17
 Maseda M. V. et al., 2018, *ApJ*, 854, 29
 McLure R. J. et al., 2011, *MNRAS*, 418, 2074
 Merlin E. et al., 2021, *A&A*, 649, A22
 Momcheva I. G. et al., 2016, *ApJS*, 225, 27
 Naidu R. P., Forrest B., Oesch P. A., Tran K.-V. H., Holden B. P., 2018, *MNRAS*, 478, 791
 Naidu R. P., Tacchella S., Mason C. A., Bose S., Oesch P. A., Conroy C., 2020, *ApJ*, 892, 109
 Nakajima K., Ellis R. S., Robertson B. E., Tang M., Stark D. P., 2020, *ApJ*, 889, 161
 Oesch P. A. et al., 2018, *ApJS*, 237, 12
 Oke J. B., Gunn J. E., 1983, *ApJ*, 266, 713
 Onodera M. et al., 2020, *ApJ*, 904, 180
 Pahl A. J., Shapley A., Steidel C. C., Chen Y., Reddy N. A., 2021, *MNRAS*, 505, 2447
 Peng C. Y., Ho L. C., Impey C. D., Rix H.-W., 2002, *AJ*, 124, 266
 Ramabason L., Schaerer D., Stasińska G., Izotov Y. I., Guseva N. G., Vílchez J. M., Amorín R., Morisset C., 2020, *A&A*, 644, A21
 Rasappu N., Smit R., Labbé I., Bouwens R. J., Stark D. P., Ellis R. S., Oesch P. A., 2016, *MNRAS*, 461, 3886
 Reddy N. A., Steidel C. C., 2009, *ApJ*, 692, 778
 Reddy N. A. et al., 2015, *ApJ*, 806, 259
 Reddy N. A. et al., 2018, *ApJ*, 869, 92
 Rivera-Thorsen T. E. et al., 2017, *A&A*, 608, L4

- Roberts-Borsani G. W. et al., 2016, *ApJ*, 823, 143
 Roberts-Borsani G. W., Ellis R. S., Laporte N., 2020, *MNRAS*, 497, 3440
 Robertson B. E., Ellis R. S., Furlanetto S. R., Dunlop J. S., 2015, *ApJ*, 802, L19
 Sanders R. L. et al., 2020, *MNRAS*, 491, 1427
 Sanders R. L. et al., 2021, *ApJ*, 914, 19
 Schenker M. A., Ellis R. S., Konidaris N. P., Stark D. P., 2014, *ApJ*, 795, 20
 Schmidt K. B. et al., 2017, *ApJ*, 839, 17
 Shivaeei I. et al., 2018, *ApJ*, 855, 42
 Skelton R. E. et al., 2014, *ApJS*, 214, 24
 Smit R. et al., 2014, *ApJ*, 784, 58
 Smit R. et al., 2015, *ApJ*, 801, 122
 Speagle J. S., Steinhardt C. L., Capak P. L., Silverman J. D., 2014, *ApJS*, 214, 15
 Stanway E. R., Eldridge J. J., Becker G. D., 2016, *MNRAS*, 456, 485
 Stark D. P., 2016, *ARA&A*, 54, 761
 Stark D. P., Schenker M. A., Ellis R., Robertson B., McLure R., Dunlop J., 2013, *ApJ*, 763, 129
 Stark D. P. et al., 2015a, *MNRAS*, 450, 1846
 Stark D. P. et al., 2015b, *MNRAS*, 454, 1393
 Stark D. P. et al., 2017, *MNRAS*, 464, 469
 Steidel C. C., Giavalisco M., Dickinson M., Adelberger K. L., 1996a, *AJ*, 112, 352
 Steidel C. C., Giavalisco M., Pettini M., Dickinson M., Adelberger K. L., 1996b, *ApJ*, 462, L17
 Steidel C. C., Bogosavljević M., Shapley A. E., Reddy N. A., Rudie G. C., Pettini M., Trainor R. F., Strom A. L., 2018, *ApJ*, 869, 123
 Storey P. J., Zeppen C. J., 2000, *MNRAS*, 312, 813
 Tang M., Stark D. P., Chevallard J., Charlot S., 2019, *MNRAS*, 489, 2572
 Tang M., Stark D. P., Chevallard J., Charlot S., Endsley R., Congiu E., 2021a, *MNRAS*, 501, 3238
 Tang M., Stark D. P., Chevallard J., Charlot S., Endsley R., Congiu E., 2021b, *MNRAS*, 503, 4105
 Topping M. W., Shapley A. E., Stark D. P., Endsley R., Robertson B., Greene J. E., Furlanetto S. R., Tang M., 2021, *ApJ*, 917, L36
 Vanzella E. et al., 2008, *A&A*, 478, 83
 Vanzella E. et al., 2016, *ApJ*, 825, 41
 Vanzella E. et al., 2020, *MNRAS*, 491, 1093
 Vanzella E. et al., 2022, *A&A*, 659, A2
 van der Wel A. et al., 2011, *ApJ*, 742, 111
 Xue Y. Q. et al., 2011, *ApJS*, 195, 10
 Xue Y. Q., Luo B., Brandt W. N., Alexander D. M., Bauer F. E., Lehmer B. D., Yang G., 2016, *ApJS*, 224, 15

This paper has been typeset from a $\text{\TeX}/\text{\LaTeX}$ file prepared by the author.